Analytic Validation of a Three-Dimensional Scalar-Potential Finite-Difference Code for Low-Frequency Magnetic Induction

Trevor W. Dawson and Maria A. Stuchly
Department of Electrical and Computer Engineering
University of Victoria
Victoria, British Columbia, Canada

Abstract

This paper presents a detailed comparison of numerical and analytical calculations of the low-frequency electric and current density fields, induced by an applied uniform axial magnetic field, in an equatorially stratified sphere having the conductivity distribution $\sigma(\varphi) = \sigma_0 e^{-\lambda \cos(p\varphi)}$ with $p \in \{1, 2\}$ and $\lambda > 0$. As shown by the analytic solution, the resulting induced fields are fully three-dimensional, and the model therefore serves as a rigorous test of numerical codes.

The numerical method is a scalar-potential finite-difference scheme based on Stevenson's method for isolated conducting bodies. This computer code was recently shown to provide excellent agreement with results computed independently by a modified Finite-Difference Time-Domain method. Nevertheless, both codes share some underlying similarities, such as their common use of parallelepiped material voxels to represent the conductivity distribution, and of an edge-based staggered grid to model the electric fields. Therefore, it is of value to compare the numerical results with analytic ones.

The analytic model has a freely adjustable contrast parameter, and supports both π- and 2π-periodic conductivity distributions. Numerical and analytical results are compared for several configurations. Full three-dimensional volumetric correlation coefficients are typically of the order of 99% or better. As might be expected, the main differences occur at the surface of the sphere, where the true circumferential fields are most poorly approximated by the staircasing approximation inherent in the numerical approximation.

1 Introduction

Accurate numerical modelling of electromagnetic fields is important in many areas, perhaps particularly in the assessment of any potentially detrimental health effects of power-frequency electromagnetic fields on humans, if such effects are related to the induced electric fields and currents in tissue.

Among the numerical methods commonly used [1] to model extremely low-frequency (ELF) electromagnetic fields are the finite-difference time-domain (FDTD) [2] method, and the impedance method (IM) [3, 4, 5]. Although standard FDTD codes are powerful and general, their direct application to extremely low-frequency modelling can result in excessively long simulation times on account of the stability criterion. With appropriate modifications, however, FDTD can compute accurate decoupled electric and magnetic ELF fields in complex heterogeneous conducting bodies in relatively short (5 ns) simulation times [6]. The IM is particularly useful for induction by magnetic sources, but has several drawbacks [7], including a vastly over-determined matrix system, and difficulties in handling multiply-connected domains in three-dimensional modelling. Both the FDTD and IM are inherently vector codes, which can limit the size of the problems that they can handle.

It was recently shown [7] that ELF modelling in compact isolated conducting bodies can be handled by a simpler and more attractive scalar potential scheme based on Stevenson's Method [8]. At low frequencies, the electric field internal to the conductor can be represented in terms of a vector potential of the static limit of the applied magnetic field, plus a scalar conduction potential. The excitation for the conduction potential consists of surface injection currents driven by any applied electric field, together with a term related to the induced electromotive force, distributed throughout the conductor volume, driven by any applied magnetic field. The method has several advantages. The indeterminacy in the underlying equations is removed, and the result is a matrix system which is approximately a factor of six smaller than in the impedance method formulation of the same problem. By choosing the source term appropriately, it is possible

to treat electric and magnetic sources in a decoupled manner. Results computed by a numerical implementation of the Scalar-Potential Finite-Difference (SPFD) method [7] in a human full-body model at 7.2 mm resolution resulted in a 3-significant digit agreement with modified FDTD [6] calculations in the same model.

Although the modified FDTD and SPFD codes use drastically different formulations (full-wave vs. static potential descriptions), they nevertheless share some underlying similarities in their numerical approximations. Both codes use parallelepiped material voxels to represent the conductivity distribution, and therefore use a staircased approximation of the actual conductor shape. Both use a voxel-edge-based staggered grid approximation to the electric field. Therefore, it is of considerable value to compare the numerical results with analytic ones.

The uniformly conducting spherical model commonly used to verify ELF magnetic modelling codes is in fact not a rigorous test. The induced electric field is essentially the applied magnetic vector potential in this case. The calculation of the loop currents in an IM formulation is therefore essentially devoted to calculating the (known) vector potential.

Recently, it was shown [9] that the problem of induction by a uniform axial applied magnetic field in an equatorially stratified sphere having the conductivity distribution $\sigma(\varphi) = \sigma_0 e^{-\lambda \cos(p\varphi)}$ with $p \in \{1, 2\}$ and $\lambda > 0$ can be solved analytically. This model has p conductivity maxima and minima, and a freely adjustable contrast parameter. In the case $p = 1$ and as viewed in the plane $z = 0$, the conductivity has a single minimum on the positive x axis and a single maximum on the negative x axis. For the case $p = 2$, there are two minima, located on the positive and negative x-axes, and two maxima, located on the positive and negative y-axes. This behaviour is depicted in Figure 1. The associated conduction potential is entirely related to the conductivity gradient, and provides the deviation in the fields from those in the uniformly conducting case, which are driven only by the applied vector potential. The observed current distribution for moderate and greater conductivity contrasts typically has a vortex, associated with each conductivity maximum, which intercepts the sphere surface at high latitudes. The fields are fully three-dimensional, and the model therefore serves as a rigorous test for numerical codes.

In this paper, results computed by the SPFD method are compared to analytical ones for several values of the parameters. It will be seen in Section 3 that the numerical and analytical results are generally in excellent agreement. For example, full three-dimensional volumetric correlation coefficients between fields are mostly of the order of 99% or better. As might be expected, the main

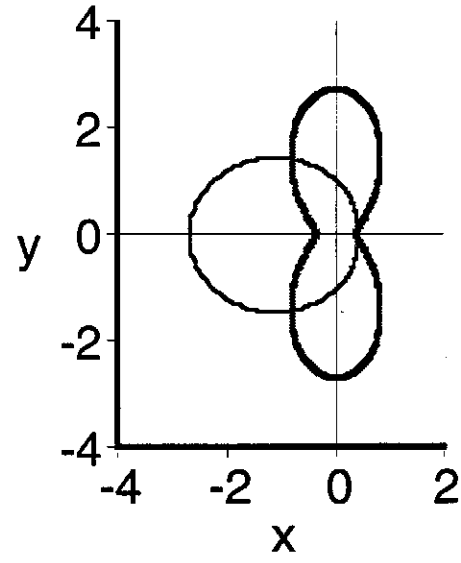

Figure 1: Polar diagrams of representative conductivity distributions in the $z = 0$ plane for $\sigma_0 = 1$ Sm^{-1} and $\lambda = 1$. The thin black curve and thick gray curve pertain to $p = 1$ and $p = 2$ respectively. The units indicated on the axes are Sm^{-1}.

differences occur at the surface of the sphere, where the true circumferential fields are most poorly approximated by the staircasing approximation inherent in the numerical approximation.

2 Summary of the SPFD Method and the Analytical Solution

2.1 Stevenson's Method

A three-dimensional domain is described in terms of Cartesian coordinates (x, y, z) with associated unit vectors $\{\hat{\boldsymbol{x}}, \hat{\boldsymbol{y}}, \hat{\boldsymbol{z}}\}$, so that a typical position vector is $\boldsymbol{r} = x\,\hat{\boldsymbol{x}} + y\,\hat{\boldsymbol{y}} + z\,\hat{\boldsymbol{z}}$. A compact body, having a maximum diameter L and electrical conductivity and permittivity distributions $\sigma(\boldsymbol{r})$ and $\varepsilon(\boldsymbol{r})$ respectively, is located in this domain, and subjected to incident time-harmonic electric and magnetic fields $\boldsymbol{E}^e(\boldsymbol{r})\, e^{+i\omega t}$ and $\boldsymbol{B}^e(\boldsymbol{r})\, e^{+i\omega t}$ of angular frequency ω. It is assumed that the inducing frequency is sufficiently low (quasi-static) that the body is much smaller than both the free-space wavelength, $L \ll \lambda \equiv 2\pi/k_0 = 2\pi c/\omega$ and the skin depth, $L \ll \delta \equiv [\omega\mu_0\sigma(\boldsymbol{r})/2]^{-1/2}$, and that conduction currents completely

dominate displacement currents, $\sigma(\boldsymbol{r}) \gg \omega\varepsilon(\boldsymbol{r})$. The permittivity distribution plays no further role in the present analysis. Since the body is non-magnetic, the magnetic permeability has its vacuum value $\mu_0 = 4\pi \times 10^{-7}$ Hm^{-1} everywhere.

Under these quasi-static assumptions, Stevenson's method [8] can be applied. Each of the incident, scattered and interior electromagnetic fields can be expanded near the conductor in a power series involving the parameter $(-ik_0)$, where $k_0 = \omega/c$ denotes the vacuum wavenumber of the fields, and $c = (\varepsilon_0\mu_0)^{-1/2} \approx 2.998 \times 10^8 \text{ms}^{-1}$ is the vacuum speed of light. As explained by Van Bladel [8], the zeroth-order interior electric field in the series expansion is zero due to the induced surface charge distribution, and the interior magnetic field is equal to the zeroth-order applied magnetic field.

If the external zeroth-order electric field is ignored (electric and magnetic fields are commonly viewed as decoupled in the low frequency limit; moreover, by choosing the source to consist of two plane waves propagating in opposite directions with appropriate phasing, the electric fields can be made to cancel in the vicinity of the sphere [6]), then the surface charge density on the sphere is zero, and the complex amplitude of the first-order internal electric field may be shown [7, 8] to have the representation

$$\boldsymbol{E}_1^i(\boldsymbol{r}) = -\nabla\psi(\boldsymbol{r}) - i\omega\boldsymbol{A}_0(\boldsymbol{r})\,, \qquad (2.1)$$

where $\boldsymbol{A}_0(\boldsymbol{r})$ is a vector potential for the zeroth-order applied magnetic field amplitude,

$$\boldsymbol{B}_0^e(\boldsymbol{r}) = \nabla \times \boldsymbol{A}_0(\boldsymbol{r})\,. \qquad (2.2)$$

The conduction potential has to satisfy the differential equation

$$\nabla\cdot[\sigma(\boldsymbol{r})\,\nabla\psi(\boldsymbol{r})] = \nabla\cdot[-i\omega\sigma(\boldsymbol{r})\,\boldsymbol{A}_0(\boldsymbol{r})] \qquad (2.3)$$

(which arises from the condition $\nabla\cdot\boldsymbol{J} = 0$), subject to the boundary condition $E_n = 0$, i.e.,

$$\hat{\boldsymbol{n}}(\boldsymbol{r})\cdot\nabla\psi(\boldsymbol{r}) = -i\omega\hat{\boldsymbol{n}}(\boldsymbol{r})\cdot\boldsymbol{A}_0(\boldsymbol{r}) \qquad (2.4)$$

at the surface of the body. Additional constraints arise from the conditions of regularity and continuity of the electric field[8].

2.2 The SPFD Method

In the numerical implementation of the SPFD to solve equations (2.3) and (2.4), the three-dimensional computational domain is discretized into a uniform set of elementary parallelepipeds or voxels. Within each voxel the electrical properties are assumed constant. The potential method is naturally confined only to the conductor, with potentials defined at the vertices of the voxels. The electric fields are defined as a set of discrete vectors on the staggered array defined by the voxel edges, with field values defined at the edge centers. These are computed *a posteriori*, using finite differences of the potential field. To allow for physical interpretation of the results, electric field vectors are defined at the voxel centers by averaging the three sets of four parallel edge components. The magnetic vector potential contribution indicated in eq.(2.1) must also be included. The current density is then computed by multiplication by the voxel conductivity.

A finite-difference approximation for equation (2.3) at a given node can be constructed by an application of the divergence theorem to an imaginary shifted voxel with that node at its centroid. It is convenient to adopt a local indexing scheme, where the target node is labeled 0 and both the nodes and edges connected to it on the $+x$, $-x$, $+y$, $-y$, $+z$ and $-z$ sides are indexed from 1 to 6 respectively, as shown in Figure 2. Quantities associated

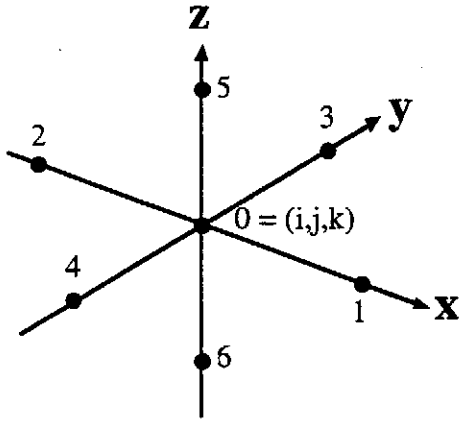

Figure 2: Local indexing scheme at a node.

with nodes or edges are then labeled with the local index of the associated object. With this shorthand, a simple finite difference equation results :

$$\left(\sum_{r=1}^{6} s_r\right)\psi_0 - \sum_{r=1}^{6} s_r\psi_r = i\omega\sum_{r=1}^{6}(-1)^{r+1}s_r\ell_r A_{0r} \qquad (2.5)$$

In this equation, ℓ_r denotes the various edge lengths in the local indexing scheme, and A_{0r} denotes the component of the external magnetic vector potential tangent to the r^{th} edge, evaluated at the edge centre. The coefficients are the edge conductances $s_r \equiv \bar{\sigma}_r a_r/\ell_r$, where $\bar{\sigma}_r$ denotes the average conductivity of the four voxels contacting edge r and a_r is the area of the voxel face normal to edge r. The above equations need to be modified in

an obvious manner if the central point is connected to less than 6 neighbouring nodes in the conductor. It may be noted here that the above equations may be viewed as modelling a Cartesian lattice of resistors associated with the voxel edges, and in this sense, the induced currents may be considered to be confined to these edges. This point of view has consequences for the surface discrepancies, observed in Section 3, between numerical and analytic calculations.

When equations of the above form are written for each vertex of every conducting voxel in the distribution, the result is a heptadiagonal system of equations which may be written as $(N - E)\, y = f$. This set of equations is diagonally dominant, symmetric, positive semi-definite. It is also singular, since the potential is indeterminate to within an additive constant. This system may be left-preconditioned to the form $(I - N^{-1}E)\, y = N^{-1}f$, or symmetrically preconditioned to the form $(I - A)\, x = b$, where $A = N^{-1/2}EN^{-1/2}$, $y = N^{-1/2}x$ and $b = N^{-1/2}f$. The singularity can be removed by augmenting the system with an equation requiring that the potential have zero mean. Either form is well-suited for solution on a computer, particularly using an iterative solvers [10]. The restarted Generalized Minimum Residual method converges well for the augmented and left-preconditioned system. However, the Conjugate Gradient Method applied to the symmetrically-preconditioned and augmented system proved to be the most efficient.

2.3 The Analytic Solution

It is assumed that the zeroth-order applied field is uniform and directed along the z-axis,

$$\boldsymbol{B}_0^e(\boldsymbol{r}) \equiv B_0 \hat{\boldsymbol{z}}, \tag{2.6}$$

so that a suitable vector potential is

$$\boldsymbol{A}_0(\boldsymbol{r}) = \tfrac{1}{2} B_0 r \sin\theta\, \hat{\boldsymbol{\varphi}}. \tag{2.7}$$

The conducting body is specialized to a sphere of radius a, centred at the origin, and having the particular positive, periodic, and equatorially stratified conductivity distribution

$$\sigma(\varphi) = \sigma_0 e^{-\lambda \cos(p\varphi)}, \tag{2.8}$$

with $p \in \{1, 2\}$ and $\lambda > 0$. This model has p conductivity maxima and minima for $-\pi < \varphi \leq \pi$, and a maximum conductivity contrast of $e^{2\lambda}$. The logarithmic derivative of the conductivity is

$$s'(\varphi) \equiv \sigma'(\varphi)\,/\sigma(\varphi) = \lambda p \sin(p\varphi). \tag{2.9}$$

Under these restrictions, the conduction potential satisfies the differential equation

$$\boldsymbol{\nabla}\cdot[\sigma(\varphi)\, \boldsymbol{\nabla}\psi(\boldsymbol{r})] = -C\sigma'(\varphi), \tag{2.10}$$

where

$$C \equiv i\omega B_0/2. \tag{2.11}$$

The external boundary (2.4) condition reduces to

$$\partial\psi(\boldsymbol{r})\,/\partial r = 0 \qquad (r = a) \tag{2.12}$$

in this case, since the magnetic potential is everywhere tangent to the sphere surface.

The solution to this problem is considered in detail elsewhere [9]. A suitable Green's function can be constructed by separation of variables, and a closed form expression for the conduction potential can then be derived. The solution has the form of the expansion

$$\psi(\boldsymbol{r}') = C \sum_{\varpi\in\{e,o\}} {\sum_{m,n=0}^{\infty}}' W_{mn}^{\varpi} \hat{F}_m^{\varpi}(\varphi')\, \hat{Q}_{mn}^{\varpi}(\theta')\, \tilde{R}_{\nu_{mn}^{\varpi}}(r'), \tag{2.13}$$

where the prime indicates that the $m = n = 0$ term is to be omitted from the sum. Here the terms $\hat{F}_m^{\varpi}(\varphi')$ denote the even and odd eigenfunctions of the equatorial differential equation

$$\left[\sigma(\varphi)\, F_\mu'(\varphi)\right]' = -\mu^2 \sigma(\varphi)\, F_\mu(\varphi), \tag{2.14}$$

under the boundary conditions of periodicity

$$F_\mu(\varphi + 2\pi) = F_\mu(\varphi), \tag{2.15}$$

and regularity, normalized with respect to the inner product

$$\langle f \,|\, g \rangle_\varphi \equiv \int_{-\pi}^{+\pi} \sigma(\varphi)\; f(\varphi)\, g(\varphi)\, d\varphi. \tag{2.16}$$

In the case $p = 2$, this equation has both π-periodic and 2π-periodic even and odd eigenfunctions, but only 2π periodic ones in the case $p = 1$. The azimuthal functions $\hat{Q}_{mn}^{\varpi}(\theta')$ have the expression

$$\hat{Q}_{mn}^{\varpi}(\theta) = \sin^\mu\theta\, C_n^{(\mu+1/2)}(\cos\theta)\,/N_{m,n}^{\varpi}, \qquad (n = 0, 1, \ldots) \tag{2.17}$$

in terms of ultraspherical polynomials, and μ denotes any one of the equatorial eigenvalues. The denominator scale factors are chosen to make the functions orthonormal with respect to the inner product

$$\langle f \,|\, g \rangle_\theta \equiv \int_0^\pi f(\theta)\, g(\theta)\, \sin\theta\, d\theta. \tag{2.18}$$

The radial functions appearing in the potential are

$$\begin{aligned} \tilde{R}_\nu(r') &= \frac{r'^2}{10}\left(1 - 2\ln\frac{r'}{a}\right), && (\nu = 2), \\ &= \left(\frac{a^2}{(\nu+3)(\nu-2)}\right)\left\{\left(\frac{r'}{a}\right)^2 - \frac{2}{\nu}\left(\frac{r'}{a}\right)^\nu\right\}, && (\nu \neq 2), \end{aligned} \tag{2.19}$$

and have zero derivative at $r' = a$, as required. The expansion coefficients in the potential involve integrals of the equatorial and azimuthal eigenfunctions,

$$W_{mn}^{\varpi} = \left\langle s' \middle| \hat{F}_m^{\varpi} \right\rangle_{\varphi} \left\langle 1 \middle| \hat{Q}_{mn}^{\varpi} \right\rangle_{\theta}. \qquad (2.20)$$

The potential can be differentiated term-by-term in spherical coordinates to get the spherical components of the electric field. These can then be converted to Cartesian components for comparison with the SPFD results.

3 Results

Comparisons were made for five test cases, using the parameters shown in Table I. The cases cover a range of conductivity contrasts for the case of a π-periodic ($p = 2$) conductivity distribution, and a single run with a 2π-periodic ($p = 1$) conductivity distribution. The actual values of the conductivity scale σ_0 and sphere radius a are relatively unimportant — they essentially reduce to an overall scale factor for the calculated fields. The table indicates the minimum and maximum conductivity values, as well as the contrast parameter (which is the ratio of maximum conductivity value to the minimum, and is given by $e^{2\lambda}$). Runs A through D of the SPFD code used $N = 100$ voxels to span the sphere diameter, while Run E was done at higher resolution, using 150 voxels. The code embeds the conductor in a parallelepiped-shaped bounding box, with an extra layer of air added on all sides for bookkeeping purposes. The row labeled "Nodes (total)" indicates the number of nodes (located at voxel vertices) in the bounding box, which is 103^3 for Runs A through D, and 153^3 for Run E. Equations are written only of those nodes contacting at least one conducting voxel. The resulting number of equations is indicated in the row labeled "Nodes (active)". In all cases, the inducing field was a 60-Hz, 1-T uniform magnetic field directed along the z-axis.

All SPFD calculations were carried out on a Hewlett-Packard 9000/735 Unix workstation with 336 megabytes of physical memory. As indicated in the Introduction, the SPFD conduction potential matrix system was found to be reliably solvable using either the restarted Generalized Minimal-Residual Method (GMRES) or the Conjugate Gradient Method [11] from the PIM package [10], running in sequential mode on the above-mentioned workstation. The latter was found to have the better performance. The primary output of the code is the values of the conduction potential at the conducting voxel vertices. Finite differences lead to electric field contributions defined at the voxel edges. These are then shifted to the voxel centroids using averages of the four edge fields parallel to each Cartesian axis. Full electric fields are then calculated by inclusion of the applied magnetic vector potential, as indicated in eq.(2.1). Current densities are simply obtained by multiplication of the resulting voxel electric field by the voxel conductivity. The corresponding analytical fields can be computed at the same locations, and the two calculations compared pointwise.

Figures 3, 4 and 5 present a graphical comparison of the fields for Run E, in the three principal Cartesian planes. The upper left panel of each figure shows the modulus of the electric field as computed using the analytic solution, while the lower left panel shows the associated current density. The right-hand panels depict the voxel-wise difference of the absolute values of the analytically and numerically calculated results. It is evident that although the individual errors can be fairly large (for example, of the order of 25% in the $z = 0$ plane of Figure 3, and 10% in the $y = 0$ and $x = 0$ planes of Figures 4 and 5 respectively), they are almost entirely confined to the surface of the sphere. In the analytic solution, the surface fields are tangential to the sphere, whereas in the staircased numerical approximation, they are essentially confined to the voxel edges. It may be noted that the conducting edge-based path length between nodes at opposite vertices of a given face (voxel) is a factor of $\sqrt{2} = 1.414$ ($\sqrt{3} = 1.732$) times greater than the corresponding hypotenuse. This effectively changes the various resistances in the numerical model relative to the analytic one. The larger surface errors are therefore perhaps not too surprising. Noticeable differences also occur near the z-axis, where the discrete conductivity values inherent in the numerical model most poorly approximate the true distribution.

Analogous illustrations of the fields for the 2π-periodic conductivity distribution of Run B are presented in Figures 6 through 8. The error pattern is similar to those observed in Run E, again being largely confined to the surface of the conductor.

To further quantify the agreement between results computed by the two methods, a set of scalar comparison descriptors is provided for the five runs in Tables II through VI. All measures are taken solely over conducting voxels. The scalar descriptors include the voxel-wise correlation ("cor.") between the analytical and numerical fields. In addition, for each method, the global minimum ("min."), maximum ("max.") and average ("avg.") values are tabulated, as well as the standard deviation ("var."). The latter is included purely as an indicator of the variation in a given field, *not* as a statistical measure. These four indicators are tabulated for the analytical ("A") results and for the numerical ("N") computations, as well as to the voxel-wise difference (analytical minus numerical, labelled "Δ") fields. Finally, these com-

Run	A	B	C	D	E
p	2	1	2	2	2
λ	3.00	1.50	2.00	0.35	1.61
σ_0 (Sm^{-1})	0.20	0.22	0.14	0.71	0.20
$\sigma_{\min}$ (Sm^{-1})	0.01	0.05	0.02	0.50	0.04
$\sigma_{\max}$ (Sm^{-1})	4.02	1.00	1.00	1.00	1.00
Contrast	403.43	20.09	54.60	2.00	25.00
a	0.50	0.50	0.25	0.50	0.50
N	100	100	100	100	150
Nodes(total)	1092727	1092727	1092727	1092727	3581577
Nodes(active)	547865	547865	547865	547865	1822023

Table I: Parameters used for the five comparison runs.

parisons were performed for each Cartesian component and magnitude of the electric field and current density distributions. Electric field and current density values are in Vm^{-1} and Am^{-2} respectively. In all cases, excitation is by a vertical 1-T, 60-Hz uniform magnetic field.

Table II details the comparisons between the numerical and analytical calculations for the high-contrast π-periodic conductivity distribution of Run A. The comparisons appear to be worse in the pointwise comparators (maximum and minimum). For example, the worst agreement is in the x component of the electric field. However, the agreement is somewhat better (about 11%) for the dominant peak values of the y-component (which is required to drive the circumferential current flow through the conductivity minima at $\varphi = 0, \pm\pi$), and the error in the peak field amplitude is about 13%. This is not surprising — the numerical electric fields are derived in part from the conduction potential, which is generated iteratively as the solution of a global set of linear equations. The solution minimizes the residual over all nodes, and the larger numerical values may be expected to affect smaller ones. There are also large discrepancies evident in the difference comparators. Similar remarks apply to the current density, although the agreement is slightly better. For example, the error in the maximum current density amplitude is about 8.6%. Note that the peak current densities appear in the x-component and are associated with the conductivity maxima.

The agreement is markedly better in the global field comparators. For example, the average and standard deviation differ in only the third significant digit for both the electric and current density fields. The three-dimensional correlation coefficients for the electric field and current density amplitudes between the two methods are 99.977% and 99.948% respectively. The poorest per-component electric correlation coefficient of 98.911% is obtained for the vertical electric field (which is entirely absent in the uniformly conducting sphere model).

Similar comments generally apply to the remaining four runs. There are perhaps only two features worthy of further explicit comment. The first concerns the poor correlations ($\approx 85\%$) for the vertical electric field and current density components in Run D as indicated in Table V. This run has a very low (2 : 1) conductivity contrast, and the vertical components are small (about 4%) compared to the peak magnitudes. Evidently, the vertical numerical fields are somewhat affected by the larger horizontal values in the iterative solution. Nevertheless, the global field comparators still indicate excellent agreement between the two methods. The second point concerns the effect of higher resolution on the numerical solution in Run E and Table VI. The addition of 50% more voxels along each axis leads to over 3 times as many unknowns in the linear system. The global comparators are perhaps only slightly better than for the other four runs. The peak values are not generally better-matched, and the effects of the staircasing approximation to the sphere surface still dominate the peak errors. Further improvement in the agreement would require the use of conformal meshing [12], for example, at the cost of additional coding complexity.

4 Closing Remarks

This paper has presented a rigorous comparison between fully three-dimensional extremely low-frequency electromagnetic fields calculated by a scalar potential finite-difference numerical code and an analytical solution. The model, consisting of an equatorially stratified sphere im-

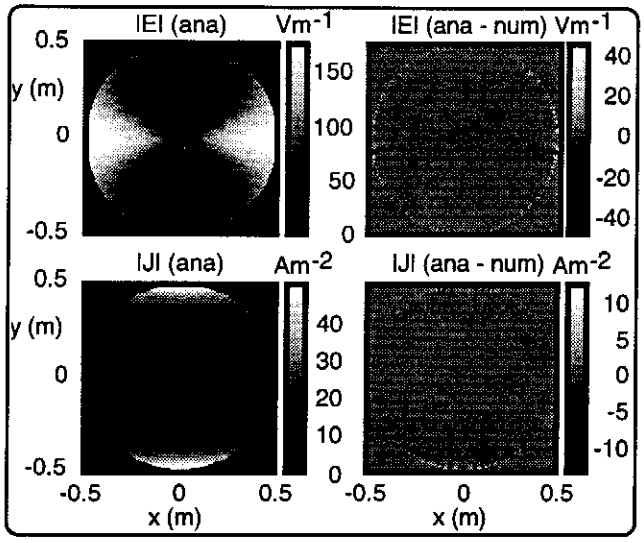

Figure 3: Field cross sections in the plane $z = 0$ for Run E (where $p = 2$).

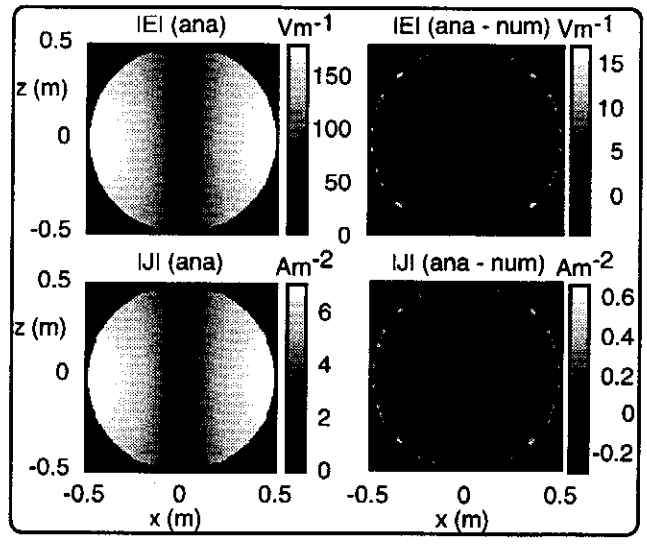

Figure 4: Field cross sections in the plane $y = 0$ for Run E.

	Field :	E_x	E_y	E_z	$\|\mathbf{E}\|$
	Cor. (%)	99.752	99.972	98.911	99.977
	Min.	−51.27	−250.67	−27.34	0.00
	Max.	51.27	250.67	27.34	250.68
A	Avg.	0.00	0.00	0.00	35.78
	Var.	14.28	65.65	5.10	57.09
	Min.	−94.27	−278.01	−35.76	0.00
	Max.	94.27	277.86	35.76	283.32
N	Avg.	0.00	−0.02	0.00	35.71
	Var.	14.28	65.54	5.12	57.01
	Min.	−64.67	−73.66	−29.02	−61.05
	Max.	64.67	73.75	29.02	57.93
Δ	Avg.	0.00	0.02	0.00	0.06
	Var.	1.01	1.55	0.75	1.44
	Field :	J_x	J_y	J_z	$\|\mathbf{J}\|$
	Cor. (%)	99.889	99.924	99.043	99.948
	Min.	−152.12	−53.58	−24.72	0.00
	Max.	152.12	53.58	24.72	152.13
A	Avg.	0.00	0.00	0.00	10.42
	Var.	16.73	14.54	3.06	19.80
	Min.	−160.95	−61.12	−26.28	0.00
	Max.	160.94	61.11	26.27	164.85
N	Avg.	0.00	0.00	0.00	10.40
	Var.	16.65	14.54	3.05	19.74
	Min.	−46.60	−42.60	−18.38	−37.58
	Max.	46.62	42.61	18.37	35.82
Δ	Avg.	0.00	0.00	0.00	0.02
	Var.	0.79	0.57	0.42	0.72

Table II: Electric field (top) and current density (bottom) comparisons for Run A. See the text for further information.

	Field :	E_x	E_y	E_z	$\|\mathbf{E}\|$
	Cor. (%)	99.930	99.964	98.726	99.973
	Min.	−91.29	−141.05	−15.83	0.00
	Max.	91.29	66.25	15.83	141.06
A	Avg.	0.00	−17.92	0.00	31.89
	Var.	26.79	39.15	3.60	39.59
	Min.	−114.65	−174.31	−21.58	0.00
	Max.	114.66	81.34	21.58	177.72
N	Avg.	0.00	−17.89	0.00	31.84
	Var.	26.74	39.08	3.62	39.53
	Min.	−39.88	−45.83	−18.89	−38.24
	Max.	39.88	36.43	18.89	36.44
Δ	Avg.	0.00	−0.03	0.00	0.05
	Var.	1.00	1.15	0.58	1.19
	Field :	J_x	J_y	J_z	$\|\mathbf{J}\|$
	Cor. (%)	99.927	99.926	98.589	99.957
	Min.	−31.88	−30.05	−6.14	0.00
	Max.	31.88	65.85	6.14	65.97
A	Avg.	0.00	0.00	0.00	7.54
	Var.	8.27	10.39	1.13	10.98
	Min.	−40.07	−30.03	−8.95	0.00
	Max.	40.07	79.92	8.95	81.55
N	Avg.	0.00	0.00	0.00	7.53
	Var.	8.26	10.36	1.14	10.96
	Min.	−19.12	−17.06	−8.79	−17.91
	Max.	19.12	21.67	8.78	16.91
Δ	Avg.	0.00	0.00	0.00	0.01
	Var.	0.32	0.40	0.19	0.39

Table III: As Table II, but for Run B.

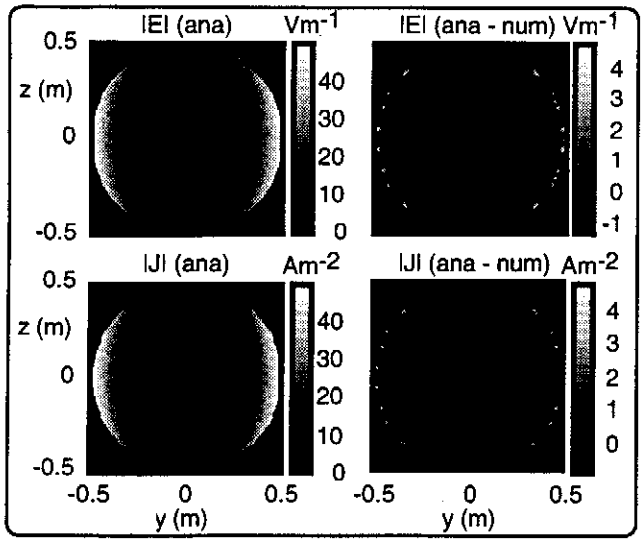

Figure 5: Field cross sections in the plane $x = 0$ for Run E.

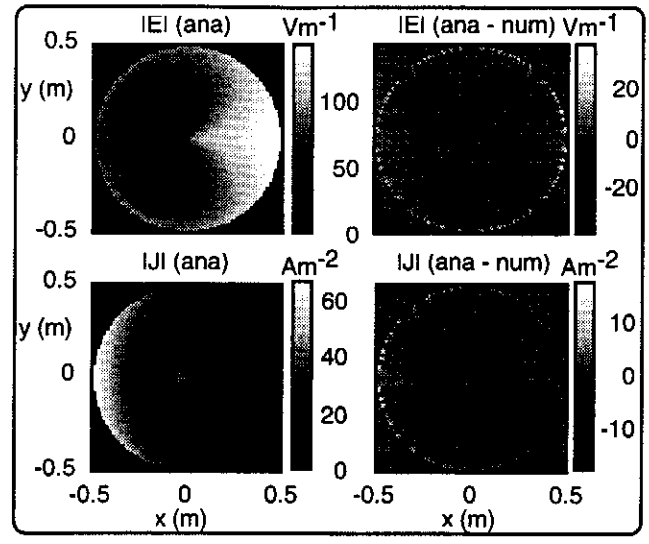

Figure 6: Field cross sections in the plane $z = 0$ for Run B (where $p = 1$).

	Field :	E_x	E_y	E_z	$\|\mathbf{E}\|$
	Cor. (%)	99.755	99.969	98.624	99.974
	Min.	−26.76	−98.59	−10.27	0.00
	Max.	26.76	98.59	10.27	98.60
A	Avg.	0.00	0.00	0.00	16.39
	Var.	6.68	28.49	2.00	24.32
	Min.	−38.84	−115.43	−14.43	0.00
	Max.	38.84	115.42	14.43	117.65
N	Avg.	0.00	0.00	0.00	16.36
	Var.	6.68	28.44	2.02	24.28
	Min.	−26.63	−30.49	−12.15	−25.31
	Max.	26.63	30.50	12.15	23.97
Δ	Avg.	0.00	0.00	0.00	0.03
	Var.	0.47	0.71	0.33	0.66
	Field :	J_x	J_y	J_z	$\|\mathbf{J}\|$
	Cor. (%)	99.891	99.927	98.902	99.948
	Min.	−22.49	−7.18	−3.11	0.00
	Max.	22.49	7.18	3.11	22.50
A	Avg.	0.00	0.00	0.00	2.12
	Var.	2.91	2.48	0.46	3.22
	Min.	−25.21	−9.23	−3.46	0.00
	Max.	25.21	9.23	3.46	25.78
N	Avg.	0.00	0.00	0.00	2.11
	Var.	2.90	2.48	0.46	3.21
	Min.	−7.12	−6.41	−2.83	−5.79
	Max.	7.12	6.41	2.83	5.50
Δ	Avg.	0.00	0.00	0.00	0.00
	Var.	0.14	0.09	0.07	0.12

Table IV: As Table II, but for Run C.

	Field :	E_x	E_y	E_z	$\|\mathbf{E}\|$
	Cor. (%)	99.926	99.953	84.908	99.966
	Min.	−80.04	−109.42	−4.09	0.00
	Max.	80.04	109.42	4.09	109.43
A	Avg.	0.00	0.00	0.00	27.62
	Var.	24.75	34.90	0.84	32.69
	Min.	−99.07	−134.93	−15.33	0.00
	Max.	99.08	134.93	15.33	137.58
N	Avg.	0.00	0.00	0.00	27.57
	Var.	24.70	34.83	0.99	32.62
	Min.	−31.19	−35.74	−14.63	−29.75
	Max.	31.20	35.75	14.63	28.36
Δ	Avg.	0.00	0.00	0.00	0.05
	Var.	0.95	1.07	0.52	1.12
	Field :	J_x	J_y	J_z	$\|\mathbf{J}\|$
	Cor. (%)	99.935	99.947	85.148	99.964
	Min.	−79.54	−54.89	−3.01	0.00
	Max.	79.54	54.89	3.01	79.78
A	Avg.	0.00	0.00	0.00	19.17
	Var.	20.85	20.81	0.60	22.38
	Min.	−97.48	−68.56	−10.08	0.00
	Max.	97.49	68.57	10.08	99.45
N	Avg.	0.00	0.00	0.00	19.14
	Var.	20.81	20.77	0.70	22.34
	Min.	−26.16	−22.95	−10.69	−21.69
	Max.	26.15	22.95	10.69	20.63
Δ	Avg.	0.00	0.00	0.00	0.03
	Var.	0.75	0.68	0.37	0.79

Table V: As Table II, but for Run D.

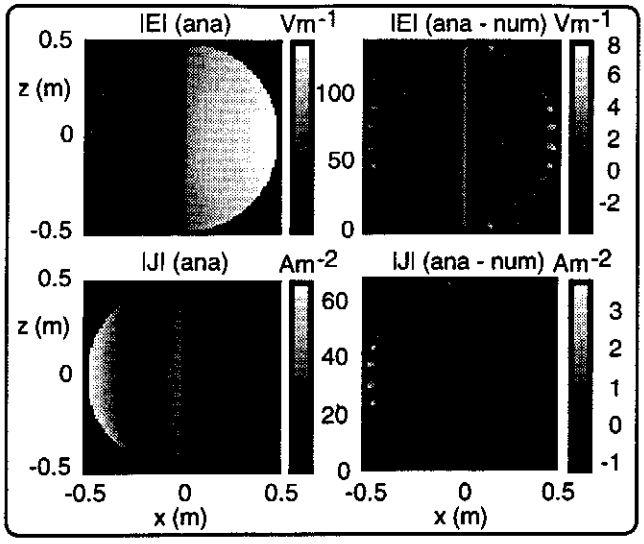

Figure 7: Field cross sections in the plane $y = 0$ for Run B.

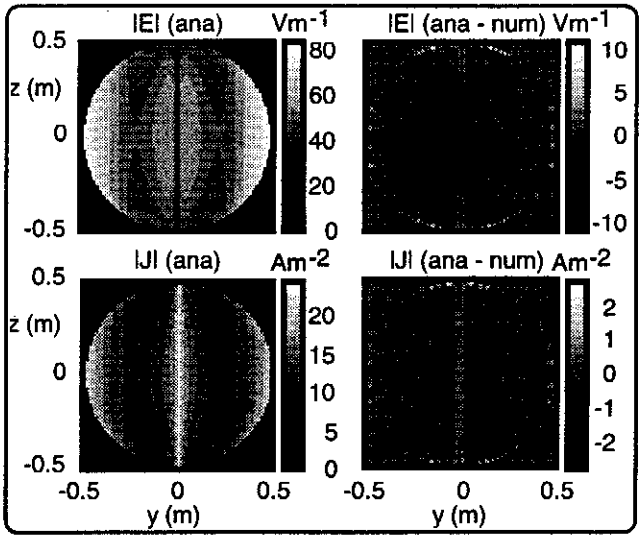

Figure 8: Field cross sections in the plane $x = 0$ for Run B.

	Field :	E_x	E_y	E_z	$\|\mathbf{E}\|$
	Cor. (%)	99.863	99.978	98.853	99.981
	Min.	−55.12	−176.58	−17.37	0.00
	Max.	55.12	176.58	17.37	176.59
A	Avg.	0.00	0.00	0.00	32.00
	Var.	14.31	53.19	3.45	44.97
	Min.	−72.51	−214.41	−26.73	0.00
	Max.	72.51	214.39	26.73	218.18
N	Avg.	0.00	0.00	0.00	31.97
	Var.	14.29	53.14	3.47	44.93
	Min.	−50.21	−54.69	−24.24	−47.80
	Max.	50.21	54.70	24.24	45.31
Δ	Avg.	0.00	0.00	0.00	0.03
	Var.	0.75	1.12	0.52	1.07
	Field :	J_x	J_y	J_z	$\|\mathbf{J}\|$
	Cor. (%)	99.930	99.957	99.124	99.966
	Min.	−49.91	−15.45	−6.12	0.00
	Max.	49.91	15.45	6.12	49.91
A	Avg.	0.00	0.00	0.00	5.69
	Var.	7.16	6.31	0.98	7.72
	Min.	−59.22	−20.13	−7.79	0.00
	Max.	59.22	20.13	7.79	60.34
N	Avg.	0.00	0.00	0.00	5.68
	Var.	7.14	6.31	0.98	7.71
	Min.	−15.43	−14.60	−6.96	−13.54
	Max.	15.43	14.60	6.97	12.69
Δ	Avg.	0.00	0.00	0.00	0.01
	Var.	0.27	0.19	0.13	0.25

Table VI: As Table II, but for Run E.

mersed in an axial quasi-uniform magnetic field, has a complex field pattern with a curved vortex system associated with each conductivity maximum. In particular, significant vertical fields can occur, in contrast to the uniformly conducting case. It has been shown that the numerical solution generally provides excellent global agreement, apart from significant discrepancies at the sphere boundary. Here the staircasing approximation inherent in the Cartesian-coordinate-based numerical code provides a poor representation to the true tangential current paths, and so leads to the observed errors.

Acknowledgment :

The authors thank the anonymous reviewers for their suggested improvements to this paper. The financial support of this research by NSERC, B.C. Hydro, TransAlta Utilities and Ontario Hydro is gratefully acknowledged.

References

[1] Om P. Gandhi. Some numerical methods for dosimetry: Extremely low frequencies to microwave frequencies. *Radio Science*, **30**(1):161–177, January-February 1995.

[2] Om P. Gandhi and Jin-Yuang Chen. Numerical dosimetry at power-line frequencies using anatomically based models. *Biolelectromagnetics Supplement*, 1:43–60, 1992.

[3] Om P. Gandhi, John F. DeFord, and Hiroshi Kanai. Impedance method for calculation of power deposition patterns in magnetically induced hyperthermia. *IEEE. Trans. Biomedical Engineering*, **BME-31**(10):644–651, October 1984.

[4] Niel Orcutt and Om P. Gandhi. A 3-D impedance method to calculate power deposition in biological bodies subjected to time varying magnetic fields. *IEEE. Trans. Biomedical Engineering*, **35**(8):577–583, August 1988.

[5] Weiguo Xi, Maria A. Stuchly, and Om P. Gandhi. Induced electric currents in models of man and rodents from 60 Hz magnetic fields. *IEEE Trans. Biomed. Eng.*, **BME-41**(11):1018–1023, 1994.

[6] Jan De Moerloose, Trevor W. Dawson, and Maria A. Stuchly. Application of FDTD to quasi-static field analysis. *Radio Science*, 1996. (manuscript submitted for publication).

[7] Trevor W. Dawson, Jan De Moerloose, and Maria A. Stuchly. Comparison of magnetically induced ELF fields in humans computed by FDTD and scalar potential FD codes. *Applied Computational Electromagnetics Society Journal*, 1996. (manuscript accepted for publication).

[8] J. Van Bladel. *Electromagnetic Fields*. Hemisphere Publishing Corporation, Washington D.C., revised printing edition, 1985.

[9] Trevor W. Dawson and Maria A. Stuchly. An analytic solution for verification of computer models for low-frequency magnetic induction. *Radio Science*, 1996. (manuscript submitted for publication).

[10] R.D. da Cunha and T.R. Hopkins. PIM 2.0 : Parallel Iterative Methods package for systems of linear equations; (FORTRAN 77 version), 1993. ©1993 R.D. da Cunha, T.R. Hopkins and Computing Laboratory, University of Kent at Canterbury, Canterbury, U.K. and Centro de Processamento de Dados, Universidade Federal do Rio Grande do Sul, Porto Alegre, Brasil.

[11] John L. Volakis. EM programmer's notebook. *IEEE Antennas and Propagation Magazine*, **37**(6):94–96, 1995.

[12] Richard Holland. Pitfalls of staircase meshing. *IEEE Trans. Electromagn. Compat.*, **35**(4):434–439, 1993.